

Intrinsic defects and conduction characteristics of Sc₂O₃ in thermionic cathode systems

Ryan M. Jacobs,^{*} John H. Booske,^{*,†} and Dane Morgan^{*,‡}

^{*}*Interdisciplinary Materials Science Program, University of Wisconsin-Madison,
1509 University Avenue, Madison, Wisconsin 53706, USA*

[†]*Department of Electrical and Computer Engineering, University of Wisconsin-Madison,
1415 Engineering Drive, Madison, Wisconsin 53706, USA*

[‡]*Department of Materials Science and Engineering, University of Wisconsin-Madison,
1509 University Avenue, Madison, Wisconsin 53706, USA*

Recent experimental observations indicate that bulk Sc₂O₃ (~200 nm thick), an insulator at room temperature and pressure, must act as a good electronic conductor during thermionic cathode operation, leading to the observed high emitted current densities and overall superior emission properties over conventional thermionic emitters which do not contain Sc₂O₃. Here, we employ *ab initio* methods using both semilocal and hybrid functionals to calculate the intrinsic defect energetics of Sc and O vacancies and interstitials and their effects on the electronic properties of Sc₂O₃ in an effort to explain the good conduction of Sc₂O₃ observed in experiment. The defect energetics were used in an equilibrium defect model to calculate the concentrations of defects and their compensating electron and hole concentrations at equilibrium. Overall, our results indicate that the conductivity of Sc₂O₃ solely due to the presence of intrinsic defects in the cathode operating environment is unlikely to be high enough to maintain the magnitude of emitted current densities obtained from experiment, and that presence of impurities are necessary to raise the conductivity of Sc₂O₃ to a high enough value to explain the current densities observed in experiment. The necessary minimum impurity concentration to impart sufficient electronic conduction is very small (approximately 7.5×10^{-3} ppm) and is probably present in all experiments.

I. INTRODUCTION

Electron emitter cathodes have myriad applications in military and civilian infrastructure, industrial manufacturing and advanced scientific research. They are critical components in radar, communications, broadcast media, medical imaging, materials characterization, materials processing, domestic, commercial and industrial food production, electronic warfare, and high energy physics research technologies.¹

Scandate (Sc₂O₃-containing) cathodes have attracted significant attention lately in both academic and industrial research settings due to their generally superior properties over other thermionic electron emitters. These superior characteristics include: higher electron emission, lower operating temperature, and good resistance to surface contamination.² Lower operating temperatures promote less degradation of the cathode (e.g. depletion of surface Ba by evaporation at high temperatures) which could in turn lead to longer cathode lifetimes while simultaneously generating a higher density of emitted electrons. A large supply of emitted electrons is important in applications demanding high current and high power densities such as THz-regime vacuum electronic devices (VED's).^{1,3}

Common thermionic emitters such as the dispenser B-type cathode are composed of pressed and sintered polycrystalline W powder impregnated with a precise compositional mixture of BaO, CaO and Al₂O₃, with typical molar ratios of 4-1-1 or 5-3-2. Scandate cathodes augment this composition by also including a small amount of Sc₂O₃ to the emissive mix.⁴ One drawback to scandate cathodes prepared in this fashion is an observed non-uniformity in electron emission. However, recent alterations to the cathode processing techniques appear to have helped mitigate this issue.^{5,6} In addition to the pressed and sintered dispenser-type scandate cathode, thin film and top layer scandate cathodes have also been studied. One particularly interesting recent investigation has used a polycrystalline W foil as a base with layers of sputter-deposited Sc₂O₃ and BaO on top

of the W foil.⁷ Top layer cathodes generally consist of a deposited Sc_2O_3 layer on the sintered and impregnated W powder substrate.^{8,9}

In addition to thermionic emission cathodes, Sc_2O_3 has numerous other applications. Sc_2O_3 has been used as a thin film gate oxide on GaN for high electron mobility transistors due to its high dielectric constant and better lattice matching over other gate insulators such as Gd_2O_3 , SiO_2 , and Si_3N_4 . Because of the improved lattice matching, the use of Sc_2O_3 as the gate oxide layer has improved device performance by minimizing current leakage and interface state density.¹⁰⁻¹² Due to its high refractive index, Sc_2O_3 has been shown to be a superior antireflective coating for UV laser^{13,14} and superluminescent LED applications.¹⁵ Overall, Sc_2O_3 is versatile and has attracted a great amount of interest in numerous advanced materials research fields.

This particular investigation is motivated by the recent results of experimental studies of electron emission from scandia-coated cathodes reported in Ref. 7. In Ref. 7, Sc_2O_3 was sputter deposited onto a polycrystalline W foil. BaO was subsequently deposited on top of some of the Sc_2O_3 regions in a square pattern with a final film thickness on the order of a couple hundred nanometers. The emission characteristics of the samples were studied with photoelectron emission microscopy (PEEM) and thermionic emission microscopy (THEEM). Overall, the cathode areas which contained film layers of W/ Sc_2O_3 /BaO exhibited much brighter and highly localized emission than the areas containing only W/BaO layers. The observed higher intensity corresponds to higher electron emission from the Sc_2O_3 -containing areas. These results are interesting namely because one would expect Sc_2O_3 to be insulating due to it having a large bandgap of roughly 6 eV.¹⁶⁻¹⁸ Sc_2O_3 films that are greater than 100 nm in thickness should be expected to behave as bulk-like Sc_2O_3 .

There have been numerous attempts to describe the physics behind the enhanced emission of scandate cathode systems. These theories include the formation of Sc-O dipole layers on the W surface which lower the work function,^{19,20} a semiconductor model whereby an applied potential lowers the emission barrier near the Sc_2O_3 surface,²¹ and Ba-Sc-O surface complexes that also act to reduce the work function.²²⁻²⁴ Although numerous theories currently exist, it is important to note that an unequivocal fundamental physical understanding of enhanced emission from Sc_2O_3 is still missing.

The overall purpose of this paper is to investigate mechanisms by which bulk-like Sc_2O_3 (an insulator) could act as a good conductor in the cathode environment ($T \sim 1200$ K, $P \sim 10^{-10}$ Torr). We first consider intrinsic defects by using *ab initio* methods to calculate the defect thermodynamics and effects these defects have on the electronic properties of Sc_2O_3 . We then briefly consider the role of impurities. This serves as the first step in understanding the enhanced emission for Sc_2O_3 .

II. COMPUTATIONAL METHODS AND THEORETICAL BACKGROUND

A. DFT Methods and Sc_2O_3 structure

All calculations of total supercell energies and defect energetics were performed using Density Functional Theory as implemented by the Vienna *ab initio* simulation package (VASP)²⁵ with a plane wave basis set. The electron exchange and correlation functionals were treated with the generalized gradient approximation (GGA)²⁶ and projector augmented wave (PAW)- type pseudopotentials²⁷ for both Sc and O atoms. The valence electron configuration of the Sc and O atoms utilized in all calculations were $3p^6 4s^2 3d^1$ and $2s^2 2p^4$, respectively. The plane wave cutoff energy was set to 290 eV and reciprocal space integration in the irreducible Brillouin Zone was conducted with the Monkhorst-Pack scheme.²⁸ A $4 \times 4 \times 4$ k-point mesh was used for the $1 \times 1 \times 1$ (40 atoms) primitive cell of Sc_2O_3 . Due to the high computational expense of larger supercells, a smaller k-point mesh of $1 \times 1 \times 1$ k-points was used for the $2 \times 2 \times 2$ (320 atoms) Sc_2O_3 supercell. It was verified that at higher k-point densities, the total Sc_2O_3 supercell energy changed less than 1 meV/f.u. (f.u. = formula unit), indicating that the chosen k-point densities were sufficient to ensure accurate total energies. The accuracy of the

4x4x4 k-point mesh is consistent with a previous *ab initio* study on Sc_2O_3 .²⁹ In addition to the use of GGA, the hybrid HSE functional was employed with 25% Hartree-Fock exchange.³⁰ Since the band gap underestimation prevalent in LDA and GGA can potentially affect the defect energetics and concentrations,³¹ the use of HSE will provide the most rigorous quantitative results. GGA is also implemented to obtain fast, qualitative results that still prove useful for comparison with both our calculated HSE values and GGA defect energetics of other materials in the literature.

Sc_2O_3 crystallizes in the cubic bixbyite crystal structure (space group 206, $\text{Ia}\bar{3}$). In a previous *ab initio* study²⁹ it was found that other polymorphs of Sc_2O_3 become stable under conditions of high pressure, high temperature, or a combination of both. However, the cubic bixbyite phase is thermodynamically stable at standard temperature and pressure conditions and also under typical scandate cathode operating conditions of high temperature ($T \sim 1200$ K) and low pressure ($P \sim 10^{-10}$ Torr).^{29,32} Therefore, our conditions of interest rule out all Sc_2O_3 polymorphs except the cubic bixbyite phase. Fig. 1 depicts the conventional cubic bixbyite structure of Sc_2O_3 . The primitive cell contains 40 atoms, while this conventional unit cell has 80 atoms. Sc resides on the 8b and 24d Wyckoff sites while O occupies the 48e sites. The 8b and 24d sites are both tetrahedrally coordinated by four O atoms, however the 8b sites have higher overall symmetry. The 48e sites are octahedrally coordinated by six Sc atoms. In addition, there are natively vacant anion sites at the 8a and 16c Wyckoff positions. Filling the 16c sites of the conventional unit cell with O atoms would yield a 2x2x2 fluorite structure.³³

The *ab initio* fully relaxed lattice parameters are $a = b = c = 9.871(65)$ Å and $\alpha = \beta = \gamma = 90$ degrees. These results are consistent with x-ray diffraction data³⁴ and previous *ab initio* studies on this material.^{18,29} The electronic band gap as predicted by GGA is about 3.9 eV, consistent with Ref. 29 but significantly below the experimentally determined band gap of 5.7-6 eV. However, the electronic band gap predicted by the HSE hybrid functional is 5.7 eV, within the experimentally determined range. Finally, the formation energy of Sc_2O_3 from pure Sc metal and O_2 gas (evaluated at $T = 298$ K and $P_{\text{O}_2} = 1$ atm) was calculated to be -1861 kJ/mol for GGA and -1938 kJ/mol for HSE, in reasonable agreement with the experimental result of -1908.8 kJ/mol (also for 298K and $P_{\text{O}_2} = 1$ atm).³⁵

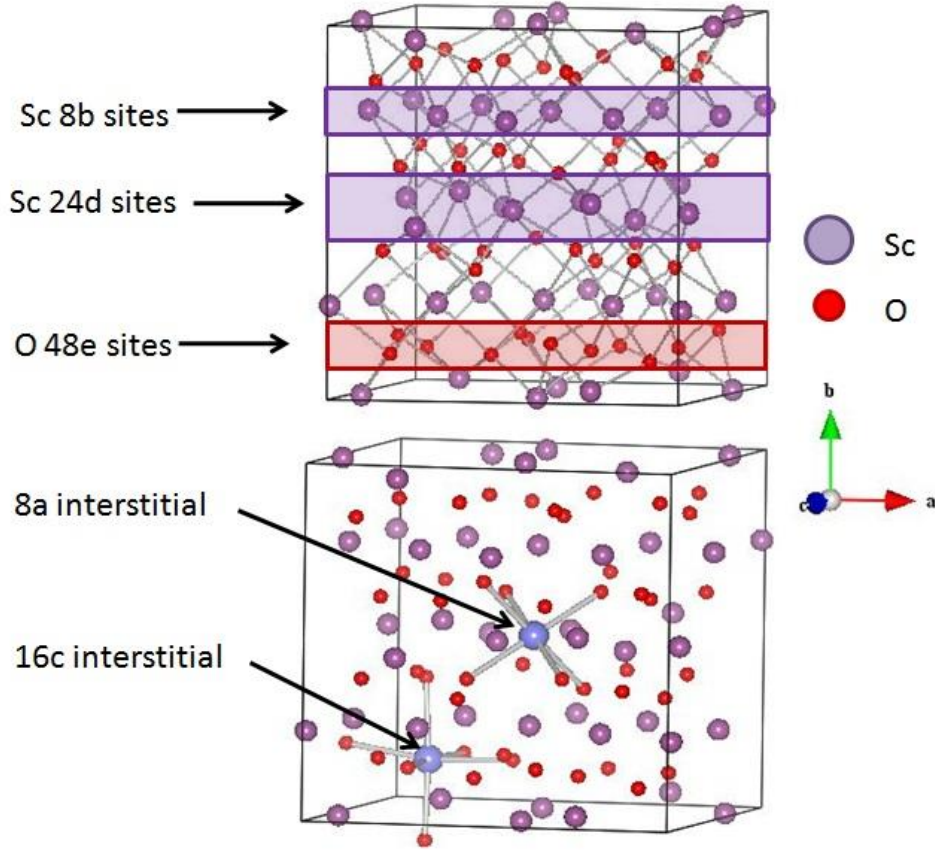


FIG. 1. Sc₂O₃ cubic bixbyite conventional unit cell depicting native and interstitial Wyckoff positions used in this study.

B. Range of Chemical Potentials

For the purposes of calculating the defect energetics and corresponding defect concentrations, it is necessary to examine the relevant range of chemical potentials for Sc and O which comprise the Sc₂O₃ system. The values of the Sc and O chemical potentials are needed to perform the defect formation energy calculations. We accomplish this by using a similar formalism as developed in previous studies.³⁶⁻⁴⁰ The chemical potentials of Sc and O depend on one another through the cohesive energy of Sc₂O₃ $E_{Sc_2O_3}^{fu}$, which is expressed (per formula unit) as:

$$2\mu_{Sc}^{Sc_2O_3} + 3\mu_O^{Sc_2O_3} = E_{Sc_2O_3}^{fu}, \quad (1)$$

and can be directly obtained from VASP calculations. In Eq. (1), $\mu_O^{Sc_2O_3}$ is the chemical potential of O in Sc₂O₃ and $\mu_{Sc}^{Sc_2O_3}$ is the chemical potential of Sc in Sc₂O₃. In the cathode operating environment of ~1200 K and 10⁻¹⁰ Torr, it is considered that Sc originates from its stable oxide (i.e. Sc₂O₃) and O originates from a reservoir of O₂ gas. This assumption is consistent with our calculations of Sc metal, which predict that Sc metal is not thermodynamically stable at 1200 K and 10⁻¹⁰ Torr (a similar Sc source was used in Ref. 22). For Sc₂O₃ to be stable with respect to Sc metal, the following inequality must hold:

$$\mu_{Sc}^{Sc_2O_3} \leq \mu_{Sc}^0, \quad (2)$$

where μ_{Sc}^0 is the chemical potential of Sc referenced to pure Sc metal. The other necessary condition for stable Sc_2O_3 is that it be stable against the loss of O:

$$\mu_O^{Sc_2O_3} \leq \mu_O^0, \quad (3)$$

where μ_O^0 is the chemical potential of O referenced to pure O_2 gas. Using Eqs. (1-3), the formation energy for Sc_2O_3 from Sc metal and O_2 gas can be expressed in terms of the above chemical potentials:

$$\Delta E_{form}^{Sc_2O_3} = 2\mu_{Sc}^{Sc_2O_3} + 3\mu_O^{Sc_2O_3} - 2\mu_{Sc}^0 - 3\mu_O^0, \quad (4)$$

Using Eq. (1) and equilibrium of O between O_2 gas and Sc_2O_3 , one can express the relevant Sc chemical potential as a function of the Sc_2O_3 cohesive energy (per formula unit) and O chemical potential:

$$\mu_{Sc}^{Sc_2O_3} = \frac{1}{2} \left(E_{Sc_2O_3}^{fu} - 3\mu_O^0 \right). \quad (5)$$

The O chemical potential can be calculated by using a combination of VASP total energies and experimental thermodynamic data for O_2 gas at the relevant reference state.⁴¹ It takes the form:⁴²

$$\mu_O^0 = \frac{1}{2} \left[E_{O_2}^{VASP} + \Delta h_{O_2}^0 + \left(H(T, P^0) - H(T^0, P^0) - TS(T, P^0) + kT \ln \left(\frac{P}{P^0} \right) - \left(G_{O_2}^{s,vib}(T) - H_{O_2}^{s,vib}(T^0) \right) \right) \right], \quad (6)$$

where $E_{O_2}^{VASP}$ is the *ab initio* calculated energy of an O_2 gas molecule, $\Delta h_{O_2}^0$ is a numerical correction for the overbinding of the O_2 molecule in DFT, $H(T, P^0)$ and $H(T^0, P^0)$ are the gas enthalpy values at standard and general temperatures T^0 and T , respectively, $S(T, P^0)$ is the gas entropy, and the logarithmic term is the adjustment of the chemical potential for arbitrary pressure. The final terms in Eq. (6), $G_{O_2}^{s,vib}$ and $H_{O_2}^{s,vib}$, shift the value of μ_O^0 to account for solid phase vibrations, which are approximated with an Einstein model with an Einstein temperature of 500 K following Refs. 24 and 42. The value of $\Delta h_{O_2}^0$ takes into account the temperature increase of O_2 gas from 0 K to T^0 , the contribution to the enthalpy at T^0 when oxygen is in the solid phase, and also corrects for the numerical error in DFT from overbinding the O_2 molecule. Because $\Delta h_{O_2}^0$ is obtained from comparing calculated formation energies and experimental formation enthalpies of numerous oxides, it is dependent on the pseudopotential and exchange/correlation functional used in the calculations. For our GGA defect energetics, we use the value of $\Delta h_{O_2}^0 = 0.33$ eV/ O_2 from Ref. 42, however no such correction has been formulated for HSE.

Fig. 2 compares the calculated formation energies of several non-transition metal oxides (with both GGA and HSE) with their respective experimental formation enthalpies. For our GGA values we obtain a value of $\Delta h_{O_2}^0 = 0.35$ eV/ O_2 . The difference of 20 meV from the result of 0.33 eV/ O_2 in Ref. 42 is due to the use of a different set of oxide materials in the calculations. For our HSE values we obtain $\Delta h_{O_2}^0 = 0.33$ eV/ O_2 . Interestingly, this shows that the DFT errors for modeling the O_2 molecule are related more to the pseudopotential used and not the exchange/correlation functional.

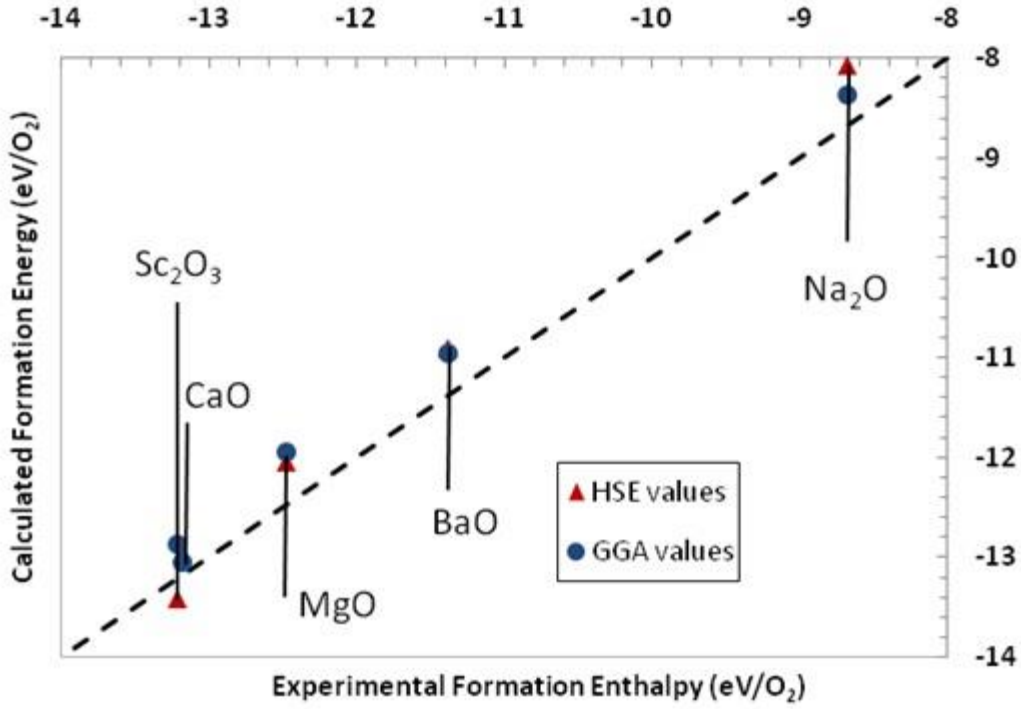


FIG. 2. Comparison of calculated formation energies to experimental formation enthalpies under standard conditions for several oxides. The average energy difference between the calculated and experimental values yields the value of $\Delta h_{O_2}^0$.

Combining Eqs. (2-4) yields the bound on the Sc chemical potential consistent with stable Sc_2O_3 and from which the defect energetics will be evaluated:

$$\mu_{Sc}^0 + \frac{1}{2} \Delta E_{form}^{Sc_2O_3} \leq \mu_{Sc}^{Sc_2O_3} \leq \mu_{Sc}^0, \quad (7)$$

This physical bound on the Sc (and thus O) chemical potentials provide an overall stability limit for Sc_2O_3 in our system. We choose three conditions within this bound to evaluate the defect energetics of the system: $\mu_{Sc}^{Sc_2O_3} = \mu_{Sc}^0$ (Sc rich conditions, high Sc partial pressure and low O partial pressure), $\mu_O^{Sc_2O_3} = \mu_O^0$ (O rich conditions, high O partial pressure and low Sc partial pressure), intermediate $\mu_{Sc}^{Sc_2O_3}$ and $\mu_O^{Sc_2O_3}$ appropriate for cathode operating conditions (T= 1200 K and P = 10^{-10} Torr). Calculation of these chemical potentials is summarized in Table I.

C. Defects in Sc_2O_3

The concentration of a crystal defect of type α at equilibrium and in the dilute limit takes the form

$$C_\alpha = N_\alpha \exp\left(\frac{-\Delta G_{form}^\alpha}{k_B T}\right), \quad (8)$$

Table I. External Sc and O chemical potentials under different conditions within the relevant chemical potential range. The values for intermediate $\mu_{Sc}^{Sc_2O_3}$ and $\mu_O^{Sc_2O_3}$ correspond to typical scandate cathode operating conditions of T=1200 K and P= 10^{-10} Torr. The GGA values are listed first and the HSE values second.

Conditions	$\mu_{Sc}^{Sc_2O_3}$ (eV/Sc)	$\mu_O^{Sc_2O_3}$ (eV/O)
O rich (Sc poor)	$\frac{1}{2}(E_{Sc_2O_3}^{f.u.} - 3\mu_O^0) =$ -16.675/ -18.284	$\mu_O^0 = -4.016/ -6.957$
Cathode operating conditions	$\frac{1}{2}(E_{Sc_2O_3}^{f.u.} - 3\mu_O^0)$ (1200 K, 10^{-10} Torr) = -13.871/ -15.480	μ_O^0 (1200 K, 10^{-10} Torr) = -5.886/ -8.827
Sc rich (O poor)	$\mu_{Sc}^0 = -6.679/ -8.228$	$\frac{1}{3}(E_{Sc_2O_3}^{f.u.} - 2\mu_{Sc}^0) =$ -10.620 / -13.661

where ΔG_{form}^α is the free energy of forming the defect, N_α is the number of sites per unit volume the defect can occupy, k_B is the Boltzmann constant and T is the absolute temperature. The free energy of formation can be expanded into

$$\Delta G_{form}^\alpha = \Delta E_{form}^\alpha - T\Delta S_{form}^\alpha + P\Delta V_{form}^\alpha, \quad (9)$$

ΔE_{form}^α is the change in total energy of the system by introduction of the defect (see Eq. (10)), ΔS_{form}^α is the formation entropy with configurational terms, which we assume is primarily due to vibrational effects, ΔV_{form}^α is the volume change when a defect is introduced, and for relevant pressures its contribution to ΔG_{form}^α can be ignored. These assumptions lead us to consider the defect formation energies as consisting of total energy differences, including the external chemical potentials and Fermi energy adjustments if the defect is charged.

In order to determine the possible role defects play in the superior emission of scandia-coated cathodes as reported in Ref. 7, the defect energetics were calculated using *ab initio* methods for the three conditions developed in Table I, and the relevant defect concentrations were calculated. Neutral and charged vacancies on the 8b and 24d Sc sites and the 48e O site were investigated. The relevant interstitial sites are at the 8a and 16c positions. Both neutral and charged Sc and O interstitials were investigated. Numerous charge states were considered in order to find the most stable charged defect species. In the case of O interstitials, charge states of 0, 1-, 2- and 3- were investigated, while charges of 0, 1+, 2+ and 3+ were used for the Sc interstitials. Sc vacancies were investigated with charge states of 0, 1-, 2- and 3- while O vacancies had charge states of 0, 1+ and 2+. Higher charge states were briefly investigated with only GGA for the 3+ O vacancy, 4+ Sc interstitial, 4- Sc vacancy and 4- O interstitial. However, these higher charge states are not stable defect charge states. In the case of the 3+ O vacancy and 4+ Sc interstitial, the defect formation energy is higher than the 2+ O vacancy and 3+ Sc interstitial under p-type conditions, indicating that these defects are not stable. In the case of the 4- Sc vacancy and 4- O interstitial, the extra charge is no longer associated with the defect, rather it is delocalized in the conduction band of the crystal, demonstrating that one cannot charge the defect to this level. Lastly, we simulated a 1+ O interstitial to examine whether a defect that typically has a negative charge could instead have a positive charge. In this case the formation energy is larger than even the neutral O interstitial, indicating that this defect type is also unstable. Defect calculations used an isolated defect method in which only one defect was introduced per supercell, and no defect complexes or clusters were considered. Supercell sizes of 1x1x1 and 2x2x2 were used in scaling calculations to extrapolate the defect formation energies to infinite supercell size (see Eq. (12)). For the singly-charged defects, electrons were doped into the supercell if the defect was negatively charged (e.g. O interstitial) and electrons were removed from the supercell if the defect was positively charged (e.g. O vacancy). The defect formation energy ΔE_{form}^α of a general defect of type α and charge q is:

$$\Delta E_{form}^{\alpha} = E_{def}^{\alpha} - E_{perf} \pm \mu_{\alpha} + q\mu_e, \quad (10)$$

where E_{def}^{α} is the energy of the defected supercell, E_{perf} is the energy of the undefected supercell, μ_{α} is the chemical potential of the defect species (+ sign for vacancies, - sign for interstitials), and $q\mu_e$ is the electron chemical potential multiplied by the charge state of the defect. The electron chemical potential can be further developed as:

$$q\mu_e = q\left(E_{VBM} + E_{Fermi} + E_{shift}\right), \quad (11)$$

where E_{VBM} is the energy of the valence band maximum, E_{Fermi} is the Fermi energy referenced to the bulk undefected supercell, and E_{shift} is the electrostatic potential energy shift. For convenience, the Fermi level is referenced to the valence band maximum in all defect calculations. The electrostatic energy shift serves as a correction for the shift of the valence band maximum by introduction of charged defect species in a finite sized supercell. Different values of E_{shift} can be applied from the VASP calculations, and for our calculations we use a modified version of the method employed by Lany and Zunger in Ref. 43. In their work, the electrostatic energy shift was obtained by calculating the average difference between the atomic-site electrostatic potentials of the defected and perfect supercells, excluding the immediate neighbors of the defect. Our method uses this averaging technique, however we also include the potentials of the nearest neighbor atoms to the defect, as this method was found to be the most accurate correction for our system.⁴⁴ Overall, the energy scale of the electrostatic energy shift is small, on the order of 10^{-3} to 10^{-1} eV, so the exact method of treating this shift will not qualitatively impact our results.

In addition to this correction for the shifting of the valence band maximum from that of the perfect supercell, the defect formation energies must also be corrected for the finite size effects of the supercell approach. Although the isolated defect method reduces defect-defect interactions within the supercell, there are still spurious strain and electrostatic interactions between the periodic supercell images. The charge corrections, first developed by Leslie and Gillan⁴⁵ and further by Makov and Payne⁴⁶ (which scale as $1/L$ and $1/L^3$) and the strain corrections (which also scale as $1/L^3$)⁴⁷ can be simplified to the form in Refs. 44,48,49. Thus, the general dependence of defect formation energy with supercell size can be expressed as:

$$\Delta E_{form,sc}^{\alpha} = \Delta E_{form,infinite}^{\alpha} + a\left(\frac{1}{L}\right) + b\left(\frac{1}{L^3}\right), \quad (12)$$

where $\Delta E_{form,sc}^{\alpha}$ is the defect formation energy in the supercell, $\Delta E_{form,infinite}^{\alpha}$ is the defect formation energy of a hypothetical infinite crystal, L is the supercell size, and a and b are fitting constants. The inverse cubic term is sufficiently small that we ignore it in our finite size scaling. The constants a and b are sometimes represented as analytic electrostatic expressions which incorporate the Madelung constant of the supercell, the dielectric constant of the material and the defect charge. However, these purely electrostatic expressions have been shown to be unreliable for numerous systems, as elastic effects are ignored and the effects of defect charge are oversimplified.⁵⁰⁻⁵² We thus follow the methods used in Refs. 44,48,52 to obtain more realistic defect formation energies in the dilute limit. By running both the 1x1x1 and 2x2x2 supercells, two defect formation energies are obtained (effectively for two different defect concentrations, since the supercell size is changing). Therefore, these two formation energies define a linear plot of $\Delta E_{form,sc}^{\alpha}$ versus $1/L$ where the constant a is the slope and $\Delta E_{form,infinite}^{\alpha}$ is the y-intercept. The value of $\Delta E_{form,infinite}^{\alpha}$ is the defect formation energy in the dilute limit. We

assume that the b/L^3 term makes a minimal contribution as the larger calculation cells needed for fitting this term are not computationally practical at this time.

III. RESULTS AND DISCUSSION

Table II contains the GGA and HSE defect formation energies for every defect calculated under the different external conditions listed in Table I. Fig. 3 consists of the data from Table II plotted as a function of the Fermi energy for the case of intermediate $\mu_{Sc}^{Sc_2O_3}$ and $\mu_O^{Sc_2O_3}$ appropriate for cathode operating conditions. The defect formation energy is a function of the Fermi energy and varies linearly with the charge state of the defect in question. Plots such as those shown in Fig. 3 are very useful when analyzing intrinsic defects because it allows one to easily see which defect species are the most stable based on the position of the Fermi energy in equilibrium. The position of the Fermi energy can be dictated by several things, such as external dopants, electrical contact with another material, or simply from the presence of intrinsic crystal defects. For our study we focus on calculating the position of the Fermi energy from the presence of just intrinsic defects in Sc_2O_3 under equilibrium conditions. From inspection of the plots in Fig. 3 one can predict that, to a first approximation, the equilibrium Fermi energy should lie in close proximity to a crossover point where the lowest energy defect types of opposite charge states have the same formation energy. This can be reasoned based solely on the fact that the entire system must remain charge neutral.

To calculate the equilibrium defect concentrations and corresponding electronic properties which arise due to the presence of these defects, we employ similar methods as detailed in Refs. 53,54 to model the defect concentration equations and Ref. 55 for the electron and hole concentrations. The relationships between the electron concentration in the conduction band and the hole concentration in the valence band and the Fermi energy are given by:

$$[e^-] = n_c(T) = N_c(T) \exp\left(\frac{-(E_{CBM} - E_{Fermi})}{k_B T}\right), \quad (13)$$

$$[h^+] = p_v(T) = P_v(T) \exp\left(\frac{-(E_{Fermi} - E_{VBM})}{k_B T}\right), \quad (14)$$

where E_{CBM} is the energy at the conduction band minimum (taken as the calculated band gap, $E_{gap} = 3.9$ or 5.7 eV for GGA and HSE, respectively), E_{VBM} is the energy at the valence band maximum (taken as equal to 0 eV), and $N_c(T)$ and $P_v(T)$ are the effective densities of states in the conduction and valence bands, respectively, and were calculated using density of states data for a perfect $1 \times 1 \times 1$ Sc_2O_3 supercell. The method of determining these effective densities of states can be found in Ref. 55 and won't be repeated here. Summing the concentrations from acceptor-type defects (negative charge) and donor-type defects (positive charge) along with their compensating electrons and holes gives the condition of charge neutrality for the system:

$$2[V_{O48e}^{2+}] + 3[Sc_{i,16c}^{3+}] + 3[Sc_{i,8a}^{3+}] + [h^+] = 2[O_{i,16c}^{2-}] + 2[O_{i,8a}^{2-}] + 3[V_{Sc8b}^{3-}] + 3[V_{Sc24d}^{3-}] + [e^-], \quad (15)$$

Substituting Eqs. (8), (13) and (14) into Eq. (15) and solving yields a single self-consistent value for the Fermi energy at equilibrium that ensures that both charge neutrality and electron/hole mass action are obeyed. From this, the equilibrium concentrations for all defect types, electrons and holes can be calculated.

Table III summarizes the equilibrium concentrations for intrinsic defects in Sc_2O_3 under cathode operating conditions (intermediate $\mu_{Sc}^{Sc_2O_3}$ and $\mu_O^{Sc_2O_3}$ for both GGA and HSE defect formation energy values). The values for the intrinsic Fermi level $E_{Fermi,intrinsic}$ and intrinsic carrier concentration n_i for a perfect crystal of Sc_2O_3 are given as a point of comparison to the values obtained when defects are present, and were calculated using both the GGA and HSE density of states data and the calculated E_{gap} values of 3.9 eV (GGA) and 5.7 eV (HSE). In both the GGA and HSE cases, the dominant defect types are O interstitials on the 16c Wyckoff site, giving rise to an excess of holes in the valence band. The equilibrium hole concentration is roughly 3 orders of magnitude larger than the intrinsic (thermally generated) carrier concentration for GGA and 4 orders of magnitude larger when HSE defect formation energies are used, indicating that under cathode operating conditions bulk Sc_2O_3 should behave as a p-type semiconductor.

To the best of our knowledge, there is no experimental data for electron or hole mobility in Sc_2O_3 . To understand how well Sc_2O_3 will conduct under cathode operating conditions solely from intrinsic defects, we use our calculated hole concentrations at equilibrium and calculate ballpark conductivity values based on the mobility of other oxide materials. A survey of mobility values for ZnO, SnO_2 , SiO_2 , In_2O_3 , ZrO_2 , UO_2 , BaO and TiO_2 yielded values between 10^{-2} to 10^3 $cm^2/V\cdot s$.⁵⁶⁻⁶³ From some extrapolation of the data trends presented for the above list of oxides, the mobility at high T for polycrystalline oxide samples is roughly between 10^{-2} to 1 $cm^2/V\cdot s$.

Table II. GGA and HSE ΔE_{form}^α for various defect types under the different Sc and O external conditions developed above. Both the GGA and HSE values have been corrected for finite size effects. In the formation energy columns, the GGA value is listed first and the HSE value second. All formation energies are referenced to the VBM.

Defect	Charge on defect	Kröger-Vink notation	ΔE_{form}^α (Sc rich) (eV)	ΔE_{form}^α (O rich) (eV)	ΔE_{form}^α (intermediate $\mu_{Sc}^{Sc_2O_3}$ and $\mu_O^{Sc_2O_3}$) (eV)
V_{Sc8b}	0	V_{Sc}^x	13.311 / 16.681	3.406 / 6.625	6.209 / 9.429
V_{Sc8b}	-1	V_{Sc}'	13.394 / 17.055	3.488 / 6.999	6.292 / 8.832
V_{Sc8b}	-2	V_{Sc}''	13.584 / 17.513	3.678 / 7.457	6.483 / 9.089
V_{Sc8b}	-3	V_{Sc}'''	14.056 / 18.297	4.150 / 8.241	6.957 / 9.465
V_{Sc24d}	0	V_{Sc}^x	13.317 / 16.413	3.412 / 6.357	6.216 / 9.161
V_{Sc24d}	-1	V_{Sc}'	13.355 / 16.794	3.449 / 6.738	6.254 / 9.542
V_{Sc24d}	-2	V_{Sc}''	13.493 / 17.258	3.587 / 7.202	6.393 / 10.006
V_{Sc24d}	-3	V_{Sc}'''	14.232 / 18.477	4.327 / 8.421	7.138 / 11.224
V_{Sc24d}	-4	V_{Sc}''''	17.742 / n/a	7.746 / n/a	10.550 / n/a
V_{O48e}	0	V_O^x	0.837 / 0.944	7.441 / 7.648	5.571 / 5.779
V_{O48e}	+1	V_O^\bullet	-1.900 / -2.555	4.704 / 4.149	2.835 / 2.280
V_{O48e}	+2	$V_O^{\bullet\bullet}$	-4.563 / -6.284	2.041 / 0.420	0.174 / -1.449
V_{O48e}	+3	$V_O^{\bullet\bullet\bullet}$	-4.496 / n/a	2.109 / n/a	0.239 / n/a

$Sc_{i,8a}$	0	Sc_i^x	4.289 / 5.585	14.194 / 15.641	11.389 / 12.837
$Sc_{i,8a}$	+1	Sc_i^\bullet	0.822 / 0.610	10.728 / 10.666	7.923 / 7.862
$Sc_{i,8a}$	+2	$Sc_i^{\bullet\bullet}$	-2.296 / -3.648	7.609 / 6.408	4.806 / 3.604
$Sc_{i,8a}$	+3	$Sc_i^{\bullet\bullet\bullet}$	-5.164 / -7.956	4.742 / 2.100	1.943 / -0.704
$Sc_{i,16c}$	0	Sc_i^x	4.670 / 6.049	14.576 / 16.105	11.778 / 13.302
$Sc_{i,16c}$	+1	Sc_i^\bullet	1.012 / 0.816	10.917 / 10.872	8.120 / 8.068
$Sc_{i,16c}$	+2	$Sc_i^{\bullet\bullet}$	-2.587 / -3.933	7.319 / 6.123	4.519 / 3.319
$Sc_{i,16c}$	+3	$Sc_i^{\bullet\bullet\bullet}$	-5.626 / -8.287	4.280 / 1.769	1.476 / -1.036
$Sc_{i,16c}$	+4	$Sc_i^{\bullet\bullet\bullet\bullet}$	-5.666 / n/a	4.330 / n/a	1.526 / n/a
$O_{i,8a}$	0	O_i^x	9.229 / 10.675	2.625 / 3.971	4.495 / 5.840
$O_{i,8a}$	-1	O_i'	9.405 / 11.442	2.801 / 4.738	4.670 / 6.608
$O_{i,8a}$	-2	O_i''	9.809 / 11.882	3.205 / 5.178	5.074 / 7.047
$O_{i,8a}$	-3	O_i'''	13.506 / 17.173	6.902 / 10.470	8.771 / 12.338
$O_{i,16c}$	+1	O_i^\bullet	8.732 / n/a	2.128 / n/a	3.998 / n/a
$O_{i,16c}$	0	O_i^x	8.598 / 10.516	1.994 / 3.812	3.864 / 5.681
$O_{i,16c}$	-1	O_i'	8.558 / 10.680	1.954 / 3.976	3.823 / 5.845
$O_{i,16c}$	-2	O_i''	8.937 / 11.271	2.333 / 4.567	4.203 / 6.436
$O_{i,16c}$	-3	O_i'''	12.388 / 16.159	5.784 / 9.455	7.654 / 11.324
$O_{i,16c}$	-4	O_i''''	16.123 / n/a	9.519 / n/a	11.389 / n/a

Table III. Summary of results for solving the defect model self-consistently under cathode operating conditions.

Physical Quantity	GGA Result	HSE Result
$E_{Fermi,intrinsic}$ (eV)	2.09	2.95
n_i (cm ⁻³)	1.70x10 ¹³	3.83x10 ⁹
$E_{Fermi,equilibrium}$ (eV)	1.36	2.10
p_v (cm ⁻³)	2.00x10 ¹⁶	1.39x10 ¹³
n_c (cm ⁻³)	1.44x10 ¹⁰	1.06x10 ⁶
$[O_{i,16c}^{2-}]$ (cm ⁻³)	9.98x10 ¹⁵	7.06x10 ¹²
$[V_{O48e}^{2+}]$ (cm ⁻³)	3.49x10 ¹⁰	1.36x10 ¹¹
$[O_{i,8a}^{2-}]$ (cm ⁻³)	1.10x10 ¹²	9.60x10 ⁹
$[V_{Sc8b}^{3-}]$ (cm ⁻³)	7.04x10 ⁹	4.52x10 ⁸
$[V_{Sc24d}^{3-}]$ (cm ⁻³)	3.67x10 ⁹	55.86
$[Sc_{i,16c}^{3+}]$ (cm ⁻³)	0.08	1.25
$[Sc_{i,8a}^{3+}]$ (cm ⁻³)	4.22x10 ⁻⁴	2.52x10 ⁻²

The highest mobility value of 10³ cm²/V-s belonged to single crystal ZnO at 50 K, which has a mobility on the order of highly doped Si. The conductivities have been estimated by using the expression for the conductivity of a semiconductor as found in Ref. 55 with different mobility values for the hole densities calculated from both GGA and HSE. These conductivity values are summarized in Table IV. From Table IV we see that the highest

calculated conductivity for Sc_2O_3 under cathode operating conditions due to intrinsic defects is $3.20 \Omega^{-1}\text{cm}^{-1}$. By comparison, pure Cu has a conductivity of about $1.22 \times 10^5 \Omega^{-1}\text{cm}^{-1}$ at 1165 K,⁶⁴ which is about 5 orders of magnitude higher than the best possible conductivity value for Sc_2O_3 from intrinsic defects. In reality, the conductivity of Sc_2O_3 is most likely more than 5 orders of magnitude lower than that of Cu, because the mobility of holes in Sc_2O_3 will likely be lower than single crystal ZnO at 50K, and the carrier concentration should be closer to that predicted by HSE than GGA due to the increased robustness of the HSE DFT calculations over GGA at predicting defect formation energies.^{30,31,65,66}

Table IV. Conductivities for Sc_2O_3 using the calculated equilibrium hole concentrations from both GGA and HSE for different mobilities.

	GGA: $p_v = 2.00 \times 10^{16}$ h^+/cm^3		HSE: $p_v = 1.39 \times 10^{13}$ h^+/cm^3	
Source of Mobility	μ ($\text{cm}^2/\text{V-s}$)	σ ($1/\Omega\text{-cm}$)	μ ($\text{cm}^2/\text{V-s}$)	σ ($1/\Omega\text{-cm}$)
Bulk oxide (low)	10^{-2}	3.20×10^{-5}	10^{-2}	2.22×10^{-8}
Bulk oxide (high)	10^3	3.20	10^3	2.22×10^{-3}

Although Sc_2O_3 will not behave as a “good” electronic conductor like Cu under operating conditions, it could conduct well *enough* such that the limiting step for thermionic emission lies at the W/ Sc_2O_3 interface or at the Sc_2O_3 surface, and not conduction of electrons through bulk Sc_2O_3 . To investigate this, we consider the simple circuit model depicted in Fig. 4. This model consists of a series circuit composed of the W substrate, 200 nm Sc_2O_3 film, vacuum region, and electron collection anode. This model is essentially the idealized geometry of the cathode experiments detailed in Ref. 7. The voltage drop across the W substrate is considered negligible since W is metallic and hence a good conductor. The emission current density was approximated from data presented in Ref. 67 at 1200 K and the applied voltage of 15 kV was quoted in Ref. 7.

Using this circuit model combined with applying Ohm’s law in Region II ($J = \sigma E$) and invoking current continuity in steady state operation, we use our conductivity values from Table IV to determine the electric field and voltage drop across the Sc_2O_3 film. We ascertain whether the conductivity of Sc_2O_3 from intrinsic defects is high *enough* by asserting that the electric field drop across the Sc_2O_3 film must be well below the dielectric strength of typical insulating materials (so as to not cause breakdown), and that the voltage drop across the film will be imperceptible relative to the total applied voltage.

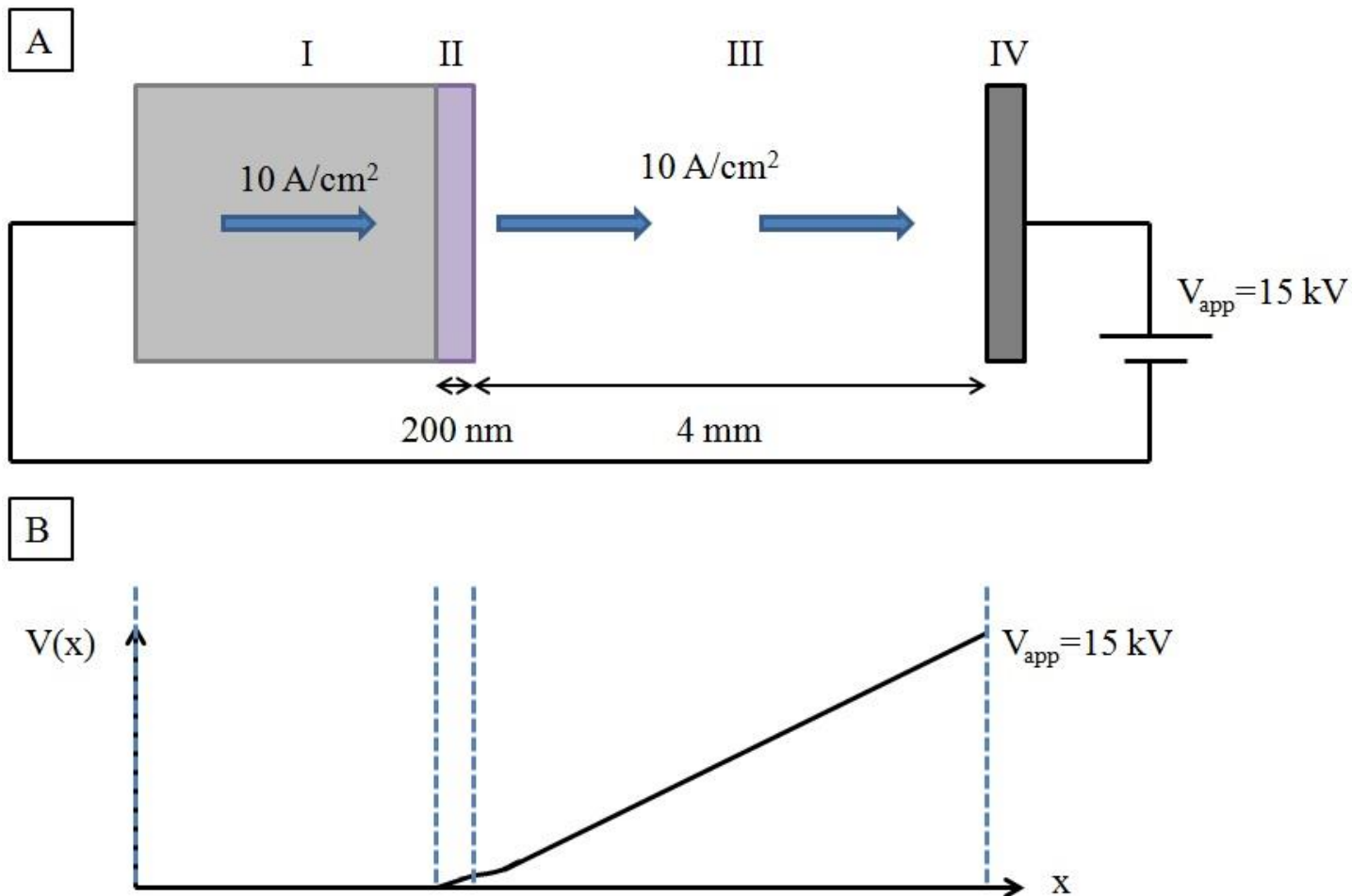


FIG. 4. (Color online) Part A: Setup of scandate cathode series circuit model. Region I is the W substrate, II is the Sc_2O_3 thin film, III is the vacuum region, and IV is the anode plate. An approximate current density of 10 A/cm^2 flows through both the cathode and vacuum region to the anode. Part B: Approximate potential $V(x)$ at different points in the circuit. It is assumed that the potential drop is linear, except near the cathode emitting surface. Near the surface, space charge depression produces a slight non-linearity in the potential.⁶⁸ The dotted lines serve as guides to the eye. Note that dimensions are not to scale.

It is necessary to maintain a small voltage drop across the Sc_2O_3 film so that the emitted electrons possess a kinetic energy that is a result of the total applied potential between the cathode and anode. If the voltage drop across the Sc_2O_3 film is a large portion of the applied potential, then the cathode will fail to yield significant electron emission. The calculated values of electric field and voltage drop across the film for different calculated conductivities are presented in Table V.

Table V. Calculated electric field and voltage drops across 200 nm Sc_2O_3 film based on a series circuit model, calculated conductivities and experimental data.

GGA: $p_v = 2.00 \times 10^{16} \text{ h}^+/\text{cm}^3$			
μ ($\text{cm}^2/\text{V}\cdot\text{s}$)	σ ($1/\Omega\cdot\text{cm}$)	E (V/cm)	V (Volts)
10^{-2}	3.20×10^{-5}	3.13×10^5	6.26
10^3	3.20	3.13	6.26×10^{-5}
HSE: $p_v = 1.39 \times 10^{13} \text{ h}^+/\text{cm}^3$			
μ ($\text{cm}^2/\text{V}\cdot\text{s}$)	σ ($1/\Omega\cdot\text{cm}$)	E (V/cm)	V (Volts)
10^{-2}	2.22×10^{-8}	4.50×10^8	9.00×10^3
10^3	2.22×10^{-3}	4.50×10^3	0.09

The dielectric strength for insulating materials ranges over one order of magnitude between roughly 5×10^4 and 5×10^5 V/cm.⁶⁹ From this, it is reasonable to assume that electric fields less than 10^5 V/cm won't cause breakdown of the Sc_2O_3 film, which results in a conductivity that must be greater than or equal to $10^{-4} \Omega^{-1}\text{-cm}^{-1}$ to sustain an emission current density of 10 A/cm². From Table V, the hole density predicted by HSE yields conductivities that are generally too low to be likely for our system. It is only for the very highest oxide mobilities that a conductivity above $10^{-4} \Omega^{-1}\text{-cm}^{-1}$ can be obtained. For a typical high-temperature oxide hole mobility of ~ 1 cm²/V-s the hole density is too small by about a factor of 50. Unless Sc_2O_3 has very exceptional hole mobility it is unlikely that the HSE predicted intrinsic carriers provide adequate conductivity for cathode emitter operation. Due to the robustness of the HSE calculation method over GGA at predicting defect formation energies (and hence defect and electron/hole concentrations) it is not reasonable to assume that Sc_2O_3 will have a hole concentration as large as 2.00×10^{16} h⁺/cm³. Rather, we conclude that HSE yields the more accurate value for the hole concentration, and thus from the arguments made above, intrinsic defects are not likely to be solely responsible for the electronic conduction in Sc_2O_3 under cathode operating conditions.

Since intrinsic defects likely provide an insufficient number of holes in Sc_2O_3 to account for the experimentally observed current densities, we propose that impurity atoms may be responsible for providing the necessary hole density to have sufficiently high conductivity while maintaining physically reasonable values of the mobility, dielectric strength, and voltage drop across the film. Since the Sc_2O_3 samples used in scandate cathodes are polycrystalline, other factors besides impurity atoms may also affect the conductivity, such as grain boundaries or regions of off-stoichiometry due to imperfect film growth. Determining the exact nature of these additional factors that affect conduction is beyond the scope of the current study, however we can still estimate the contribution of carriers from a hypothetical impurity atom, with the physically reasonable assumption that each impurity present in the Sc_2O_3 will contribute a single charge carrier to increase the conductivity. From our survey of mobility values for different oxide materials, we place a bound on the mobility of Sc_2O_3 between 10^{-2} to 10^3 cm²/V-s. Using this bound on mobility in conjunction with the current density, breakdown field, and conductivity requirements developed above, we place a bound on the required hole concentration of 6.25×10^{16} h⁺/cm³ (for $\mu = 10^{-2}$ cm²/V-s) down to 6.25×10^{11} h⁺/cm³ (for $\mu = 10^3$ cm²/V-s). With this information, we now estimate the bound on the required impurity concentration needed to raise the Sc_2O_3 conductivity to its minimum required value of $10^{-4} \Omega^{-1}\text{-cm}^{-1}$. Sc_2O_3 contains 8.32×10^{22} atoms/cm³, therefore an impurity concentration in the range 7.5×10^{-6} to 0.75 ppm (parts impurity per million lattice sites) is needed to raise the conductivity to $10^{-4} \Omega^{-1}\text{-cm}^{-1}$ for mobilities between 10^3 and 10^{-2} cm²/V-s. We note that the lowest impurity concentrations in this range are unlikely to be the required concentration as they are consistent with very exceptional mobilities for Sc_2O_3 (furthermore, as mentioned above, for such high mobilities the intrinsic defect concentrations are adequate to explain the material's conductivity). If we again consider a typical high-temperature oxide hole mobility of ~ 1 cm²/V-s an impurity concentration of 7.5×10^{-3} ppm is needed to meet the required conductivity. Sc_2O_3 samples used in experimental studies are 99.999% pure at best,^{70,71} so it is reasonable to assume that the Sc_2O_3 used in thermionic cathodes has, at best, the same purity level. A purity of 99.999% is still impure enough to have a sufficient concentration of impurities present to provide a high enough conductivity for the experimentally observed emission current densities, and this is true for any reasonable mobility of Sc_2O_3 .

IV. CONCLUSIONS

The defect energetics for intrinsic point defects in Sc_2O_3 have been investigated with DFT-based methods using both the semilocal GGA and hybrid HSE electron exchange and correlation functionals. A defect model was developed whereby the defect, electron, and hole concentrations were calculated by seeking a self-consistent value for the Fermi energy while maintaining overall charge neutrality and electron/hole mass action.

Based on these results, it is expected that Sc_2O_3 , an insulating material under room temperature and pressure conditions, will behave as a p-type semiconductor under cathode operating conditions of approximately 1200 K and 10^{-10} Torr with equilibrium hole densities of 2.00×10^{16} and $1.39 \times 10^{13} \text{ h}^+/\text{cm}^3$ for GGA and HSE, respectively.

Using these hole densities the conductivity of Sc_2O_3 was calculated using a range of mobility data from other oxide materials. A simple series circuit model was used with Ohm's law applied to the oxide film to calculate the conductivity-dependent voltage and electric field drops across a 200 nm film of Sc_2O_3 . Overall, it was reasoned that the conductivity must be greater than or equal to $10^{-4} \Omega^{-1}\text{-cm}^{-1}$ to sustain thermionic emission current densities of 10 A/cm^2 without a perceivable voltage drop or breakdown of the Sc_2O_3 film. Our results indicate that the conductivity of Sc_2O_3 solely due to the presence of intrinsic defects in the cathode operating environment is unlikely to be high enough to maintain the magnitude of emitted current densities obtained from experiment. Impurities present in a concentration range of $7.5 \times 10^{-6} - 0.75$ ppm are needed to raise the conductivity to $10^{-4} \Omega^{-1}\text{-cm}^{-1}$ for mobilities between 10^3 and $10^{-2} \text{ cm}^2/\text{V-s}$, where the impurity concentration of 7.5×10^{-3} ppm (corresponding to a mobility of $1 \text{ cm}^2/\text{V-s}$) is a reasonable value to consider for typical oxides. Therefore, a very small concentration of impurities can make the conductivity of Sc_2O_3 high enough to explain the experimentally observed current densities, and due to the very low value needed such a concentration is easily expected to exist in all experimental Sc_2O_3 samples.

ACKNOWLEDGEMENT

This work was supported by the US Air Force Office of Scientific Research, through grant numbers FA9550-08-0052 and FA9550-11-0299. This work used the Extreme Science and Engineering Discovery Environment (XSEDE), which is supported by National Science Foundation grant number OCI-1053575.

-
1. J.H. Booske, *Physics of Plasmas* **15**, 055502-16 (2008).
 2. V. Vlahos, Ph. D. Thesis, University of Wisconsin-Madison, 2009.
 3. J.H. Booske, R.J. Dobbs, C.D. Joye, C.L. Kory, G.R. Neil, P. Gun-Sik, P. Jaehun, and R.J. Temkin, *IEEE Transactions on Terahertz Science and Technology* **1**, 54-75 (2011).
 4. A. van Oostrum and L. Augustus, *Appl. Surf. Sci.* **2**, (1979).
 5. W. Yiman, W. Jinshu, L. Wei, Z. Ke, and L. Ji, *IEEE Transactions on Electron Devices* **54**, 1061-1070 (2007).
 6. W. Jinshu, L. Wei, L. Lili, W. Yanchun, W. Yiman, and Z. Meiling, *IEEE Transactions on Electron Devices* **56**, 799-804 (2009).
 7. J.M. Vaughn, K.D. Jamison, and M.E. Kordesch, *IEEE Transactions on Electron Devices* **56**, 794-798 (2009).
 8. G. Gärtner, P. Geittner, H. Lydtin, and A. Ritz, *Applied Surface Science* **111**, 11-17 (1997).
 9. J. Hasker, J. Van Esdonk, and J.E. Crombeen, *Applied Surface Science* **26**, 173-195 (1986).
 10. A.R. Kortan, N. Kopylov, J. Kwo, M. Hong, C.P. Chen, J.P. Mannaerts, and S.H. Liou, *Applied Physics Letters* **88**, 021906-3 (2006).
 11. B. Luo, *Appl. Phys. Lett.* **80**, 1661 (2002).
 12. R. Mehandru, B.P. Gila, J. Kim, J.W. Johnson, K.P. Lee, B. Luo, A.H. Onstine, C.R. Abernathy, S.J. Pearton, and F. Ren, *Electrochemical and Solid-State Letters* **5**, G51-G53 (2002).
 13. S.W. Lee, A. Daga, Z.K. Xu, and H. Chen, *Materials Science and Engineering: B* **99**, 134-137 (2003).
 14. Z. Xu, *Appl. Phys. Lett.* **79**, 3782 (2001).
 15. I. Ladany, P.J. Zanzucchi, J.T. Andrews, J. Kane, and E. DePiano, *Appl. Opt.* **25**, 472-473 (1986).
 16. A.V. Emeline, G.V. Kataeva, V.K. Ryabchuk, and N. Serpone, *The Journal of Physical Chemistry B* **103**, 9190-9199 (1999).
 17. H.H. Tippins, *Journal of Physics and Chemistry of Solids* **27**, 1069-1071 (1966).
 18. D. Richard, E.L. Munoz, T. Butz, L.A. Errico, and M. Renteria, *Physical Review B* **82**, 035206 (2010).
 19. Y. Nakanishi, T. Nagatomi, and Y. Takai, *Applied Surface Science* **256**, 1082-1087 (2009).
 20. T. Tsujita, S. Iida, T. Nagatomi, and Y. Takai, *Surface Science* **547**, 99-107 (2003).
 21. R.S. Raju and C.E. Maloney, *IEEE Transactions on Electron Devices* **41**, 2460-2467 (1994).
 22. V. Vlahos, J.H. Booske, and D. Morgan, *Physical Review B* **81**, 054207 (2010).
 23. P.M. Zagwijn, J.W.M. Frenken, U. van Slooten, and P.A. Duine, *Applied Surface Science* **111**, 35-41 (1997).
 24. V. Vlahos, Y.-L. Lee, J.H. Booske, D. Morgan, L. Turek, M. Kirshner, R. Kowalczyk, and C. Wilsen, *Applied Physics Letters* **94**, 184102-3 (2009).
 25. G. Kresse and J. Furthmuller, *Physical Review B* **54**, 11169 (1996).

26. J.P. Perdew, K. Burke, and Y. Wang, *Physical Review B* **54**, 16533 (1996).
27. G. Kresse and D. Joubert, *Physical Review B* **59**, 1758 (1999).
28. H.J. Monkhorst and J.D. Pack, *Physical Review B* **13**, 5188 (1976).
29. D. Liu, W. Lei, Y. Li, Y. Ma, J. Hao, X. Chen, Y. Jin, D. Liu, S. Yu, Q. Cui, and G. Zou, *Inorganic Chemistry* **48**, 8251-8256 (2009).
30. J. Heyd, G.E. Scuseria, and M. Ernzerhof, *The Journal of Chemical Physics* **118**, 8207-8215 (2003).
31. A. Janotti and C.G. Van de Walle, *Physica Status Solidi (B)* **248**, 799-804 (2011).
32. F. Weigel and V. Scherer, *Radiochem. Acta* **4**, (1965).
33. A. Walsh, C.R.A. Catlow, A.A. Sokol, and S.M. Woodley, *Chemistry of Materials* **21**, 4962-4969 (2009).
34. S. Geller, P. Romo, and J.P. Remeika, *Zeitschrift fur Kristallographie* **124**, 136-142 (1966).
35. J.G. Speight, *Lange's Handbook of Chemistry, 16th ed (McGraw-Hill New York)*. 2005.
36. J.R. Weber, A. Janotti, and C.G. Van de Walle, *Journal of Applied Physics* **109**, 033715-7 (2011).
37. J.X. Zheng, G. Ceder, T. Maxisch, W.K. Chim, and W.K. Choi, *Physical Review B* **73**, 104101 (2006).
38. A.F. Kohan, G. Ceder, D. Morgan, and C.G. Van de Walle, *Physical Review B* **61**, 15019 (2000).
39. J.X. Zheng, G. Ceder, T. Maxisch, W.K. Chim, and W.K. Choi, *Physical Review B* **75**, 104112 (2007).
40. D. Shrader, S.M. Khalil, T. Gerczak, T.R. Allen, A.J. Heim, I. Szlufarska, and D. Morgan, *Journal of Nuclear Materials* **408**, 257-271 (2011).
41. *NIST, in NIST Chemistry WebBook*. NIST Standard Reference Database No. 69, edited by P.J. Linstrom and W.G. Mallard (National Institute of Standards and Technology, Gaithersburg, MD, 2003), <http://webbook.nist.gov/chemistry/>.
42. Y.-L. Lee, J. Kleis, J. Rossmeisl, and D. Morgan, *Physical Review B* **80**, 224101 (2009).
43. S. Lany and A. Zunger, *Modelling and simulation in materials science and engineering* **17**, (2009).
44. S.-k. Lin, B. Puchala, Y.-L. Lee, and D. Morgan, (in preparation) (2011).
45. M. Leslie and N.J. Gillan, *Journal of Physics C: Solid State Physics* **18**, (1985).
46. G. Makov and M.C. Payne, *Physical Review B* **51**, 4014 (1995).
47. K. Garikipati, M. Falk, M. Bouville, B. Puchala, and H. Narayanan, *Journal of the Mechanics and Physics of Solids* **54**, 1929-1951 (2006).
48. B. Puchala and D. Morgan, *Physical Review B* **85**, 064106 (2012).
49. C.W.M. Castleton, A. Hoglund, and S. Mirbt, *Modeling Simul. Mater. Sci. Eng.* **17**, (2009).
50. C.W.M. Castleton, A. Höglund, and S. Mirbt, *Physical Review B* **73**, 035215 (2006).
51. J. Shim, E.-K. Lee, Y.J. Lee, and R.M. Nieminen, *Physical Review B* **71**, 035206 (2005).
52. A.F. Wright and N.A. Modine, *Physical Review B* **74**, 235209 (2006).
53. J.-P. Crocombette, D. Torumba, and A. Chartier, *Physical Review B* **83**, 184107 (2011).
54. J. Ma, S.-H. Wei, T.A. Gessert, and K.K. Chin, *Physical Review B* **83**, 245207 (2011).
55. N. Ashcroft and D. Mermin, *Solid State Physics*. 1976.
56. D.G. Schlom and L.N. Pfeiffer, *Nat Mater* **9**, 881-883 (2010).
57. R.G. Dhere, H.R. Moutinho, S. Asher, D. Young, X. Li, R. Ribelin, and T. Gessert. in *AIP Conference Proceedings*. 1999: AIP.
58. R. Hughes, *Appl. Phys. Lett.* **26**, 436 (1975).
59. R. Weiher, *J. Appl. Phys.* **33**, 2834 (1962).
60. F. Chiu, *J. Appl. Phys.* **97**, 034506 (2005).
61. S.-H. Kang, J.-H. Lee, H.-I. Yoo, H. Soo Kim, and Y. Woo Lee, *Journal of Nuclear Materials* **277**, 339-345 (2000).
62. R.N. Blumenthal, J.C. Kirk Jr, and W.M. Hirthe, *Journal of Physics and Chemistry of Solids* **28**, 1077-1079 (1967).
63. E.M. Pell, *Physical Review* **87**, 457 (1952).
64. C.E. Schuster, M.G. Vangel, and H.A. Schafft, *Microelectronics Reliability* **41**, 239-252 (2001).
65. A. Alkauskas, P. Broqvist, and A. Pasquarello, *Physical Review Letters* **101**, 046405 (2008).
66. C.G. Van de Walle and A. Janotti, *Physica Status Solidi (b)* **248**, 19-27 (2011).
67. J.M. Vaughn, K.D. Jamison, and M.E. Kordesch. in *Vacuum Electronics Conference (IVEC), 2010 IEEE International*. 2010.
68. A.S. Gilmour, *Principles of Traveling Wave Tubes*. 1994.
69. R.C. Buchanan, *Ceramic Materials for Electronics*. 2004.
70. M.F. Al-Kuhaili, *Thin Solid Films* **426**, 178-185 (2003).
71. H. Cong, H. Zhang, B. Yao, W. Yu, X. Zhao, J. Wang, and G. Zhang, *Crystal Growth & Design* **10**, 4389-4400 (2010).